

Flutter performance of box girders with wind fairings at large angles of attack

*Haojun Tang¹⁾ and Yongle Li²⁾

^{1), 2)} Department of Bridge Engineering, Southwest Jiaotong University, Chengdu
610031, China

¹⁾ thj@swjtu.edu.cn

ABSTRACT

Increasing number of long-span bridges are now constructed in complicated mountainous terrains in Southwest China where strong winds always show large angles of attack. With large angles of attack, the aerostatic and aerodynamic stability of long-span bridges shows different characteristics. Meanwhile, the aerodynamic countermeasures also have different effects on the flutter performance, which becomes one of the most important themes need to be carefully investigated. This study examines the flutter performance of box girders with wind fairings at large angles of attack based on computational fluid dynamics (CFD) simulations. The results show that a reasonable type of wind fairings could improve the flutter stability by weakening the vortex which drives the bridge to torsional vibration.

1. INTRODUCTION

Box girders with streamlined cross sections show good aerodynamic performance and have been widely used for long-span cable-supported bridges. The single box girder is a common type. For instance, the Sutong Bridge with a main span of 1088 m (Ma et al. 2018) and the Russky Bridge with a main span of 1104 m (Syrkov and Krutikov 2014) which are cable-stayed bridges, the Taizhou Yangtze River Bridge with two main spans of 2×1080 m (Tao et al. 2017) and the Great Belt Bridge with a main span of 1624 m (Larsen 1993) which are suspension bridges, are all composed of the single box girder. With the increasing bridge span, the twin-box girder has attracted great attention as this type of girders has a great potential of showing improved flutter performance and been widely adopted, such as the Xihoumen Bridge (Zhang *et al.*, 2013), the Yi Sun-sin Bridge (Lee *et al.*, 2014), and the Stonecutter Bridge (Zhu and Xu, 2014).

Wind environment is closely related to the aerostatic and the aerodynamic performance of long-span bridges. The existence of mountains has potential effects on

¹⁾ Lecturer

²⁾ Professor

the surrounding wind environment, which has attracted great attention. Even in coastal areas, the existence of hills has obvious effects on the wind environment (e.g., Bilal et al., 2016; Blocken et al., 2015; Hui et al., 2009). In complex mountainous areas, however, strong winds along rivers are blocked and deflected by mountains seriously, leading to large angles of attack (e.g., Li et al., 2017a; Li et al., 2017b; Fenerci et al., 2017; Tang et al., 2020). Attacked by large angles of attack, the box girder is likely to present bluff-body aerodynamic characteristics, which may be unfavorable to the flutter stability and has become an outstanding issue. In this situation, the wind fairing which originally was intended to let winds pass through smoothly could significantly block the flow, affecting the flutter instability. Therefore, it is very important to study the flutter performance of the box girder at large angles of attack and understand the effect of the wind fairing on the flutter performance of the bridge.

This study examines the flutter performance of box girders with wind fairings at large angles of attack based on computational fluid dynamics (CFD) simulations. The flutter derivatives of different cross sections are first extracted by CFD simulations. Taking a long-span suspension bridge as an example, the effect of the wind fairing on the critical flutter state of the bridge at large angles of attack is discussed. The flow field characteristics around the box girders during the vibration are then focused to explain how the wind fairing affects the flutter performance at large angles of attack. Finally, in section 3, some main conclusions are drawn.

2. FLUTTER PERFORMANCE AT LARGE ANGLES OF ATTACK

The Scanlan's linearized theory of flutter derivatives is widely used to estimate the critical flutter state of bridges. In this study, CFD simulations were carried out to extract the flutter derivatives of box girders and study their flutter performance.

2.1 CFD model

The cross-sectional size of box girders was simplified as a rectangular without consideration of deck secondary structures. The ratio of the girder width B to the thickness H was set to 10, 20, and 40, respectively. Then, the girder with $B/H=10$ was selected, and a pair of symmetrical wind fairings with the angle of 60° was added, as shown in Fig. 1. Fig. 1 also gives the computational domain. The length of the domain was assumed to be $17.5B$ in the mean-flow direction and $12B$ in the cross-flow direction, where B is the girder width. The windward and the leeward sides were set as the velocity-inlet and the pressure-outlet boundaries, respectively, and the sides of the girder were set as the smooth wall boundary. The distance of the girder center to the velocity inlet boundary was $5B$. Different angles of attack were simulated by changing the parameters of the velocity inlet boundary.

In order to ensure the quality of meshes around the girder during the vibration, the computational domain was divided into three regions, i.e., the rigid mesh zone, the dynamic mesh zone, and the fixed mesh zone. The rigid mesh zone moved along with the girder during the vibration. The rigid mesh zone and the fixed mesh zone were discretized by quadrilateral structured meshes, and the dynamic mesh zone was

discretized by triangular unstructured meshes. The element size progressively increased from the girder to the computational boundaries, as shown in Fig. 1. The mesh numbers for the rigid mesh zone, dynamic mesh zone, and fixed mesh zone were 62,000, 79,558, and 28,000, respectively. Unsteady Reynolds-averaged Navier-Stokes (URANS) simulations were performed by using the $k-\omega$ SST model. The discretized problem was numerically solved by utilizing a SIMPLE pressure-velocity coupling algorithm. Momentum equation, turbulent kinetic energy equation and turbulent dissipation rate equation were all solved by second order upwind schemes. The CFD software FLUENT was used in the simulations.

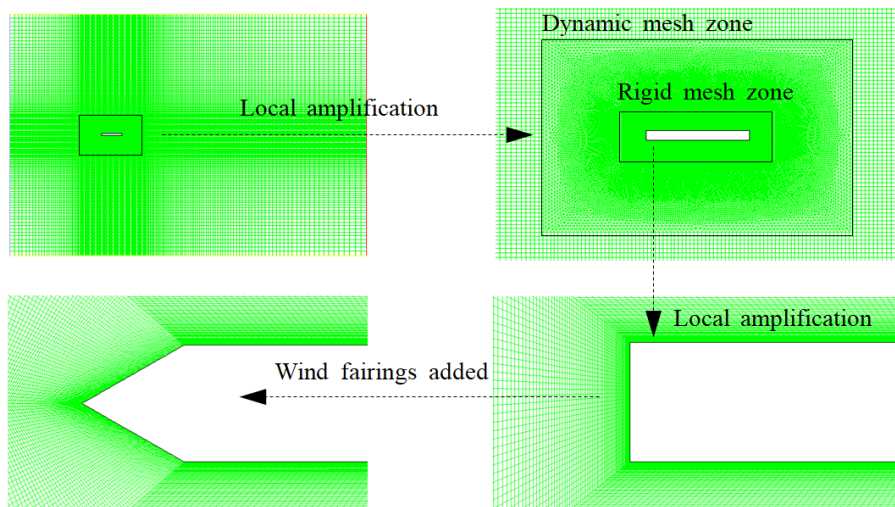


Fig. 1 Computational meshes

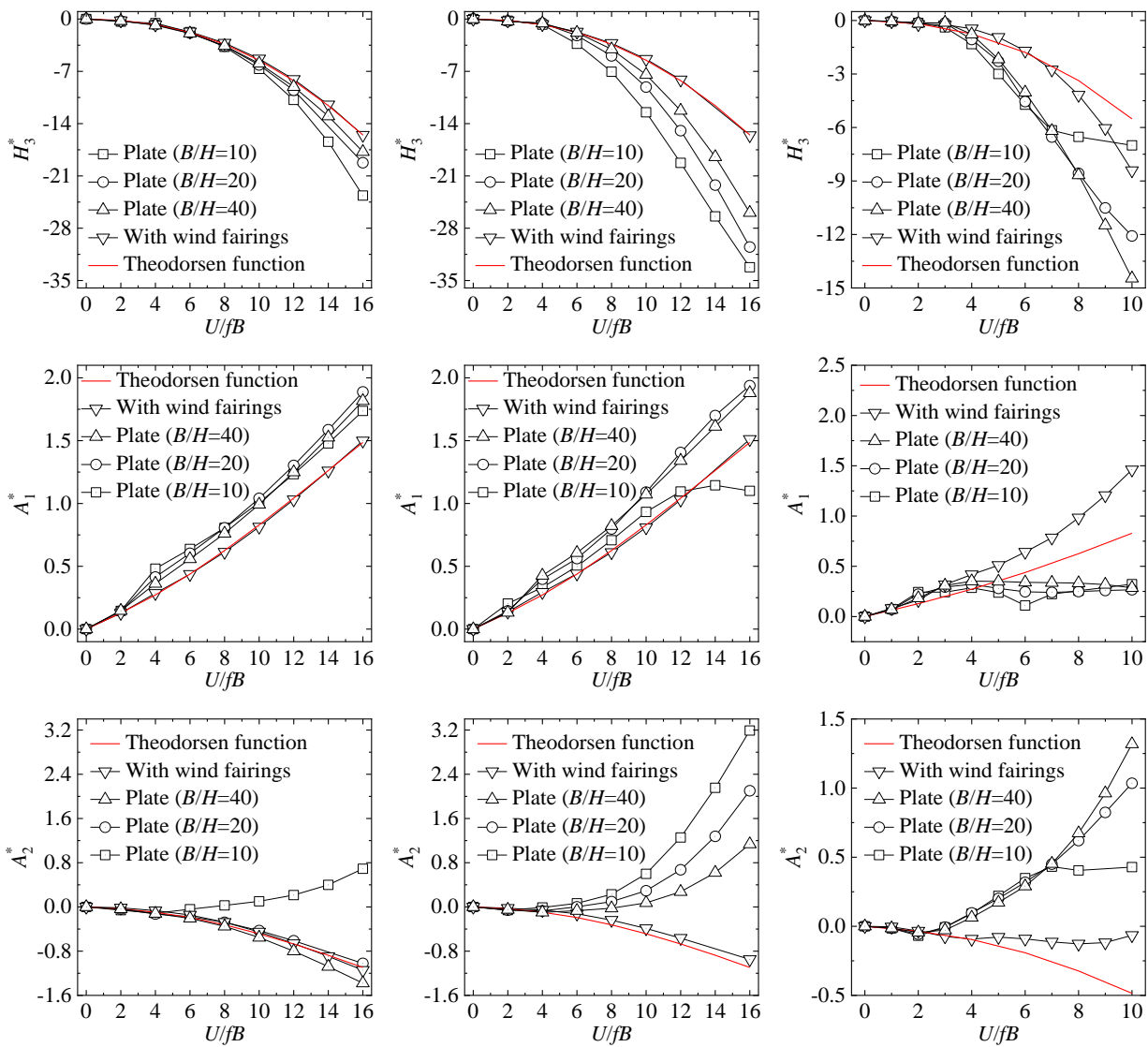
2.2 Effects of angles of attack

Single degree-of-freedom (SDOF) heaving and torsional harmonic vibrations were imposed, respectively. The amplitude of the single peak was set as $0.025B$ for heaving vibration, and 3° for torsional vibration. The vibration frequency was 2 Hz for both SDOF heaving and torsional vibrations, and the total computing time was set as 5 s with a time-step of 10^{-3} s. Four angles of attack, i.e., 0° , 4° , 8° , and 10° were taken into account, and partial results are shown in Fig. 2.

Furthermore, a suspension bridge with a main span of 1,100 m was selected to determine the critical flutter state. The natural frequencies of the symmetrical vertical and torsional modes were 0.153 Hz and 0.325 Hz, respectively. The equivalent mass and the equivalent mass moment of inertia per unit length were 3.29×10^4 kg/m and 3.32×10^6 kg·m²/m, respectively. Based on the flutter derivatives obtained by the CFD simulations, the critical flutter state of the suspension bridge was calculated via a two degree-of-freedom flutter analysis method. The damping ratio was set as zero. The critical flutter wind speeds and the flutter frequencies of the suspension bridge with different cases are shown in Fig. 3.

At null angle of attack, the flutter derivatives of the rectangles with $B/H=40$ and 20 are very close to the Theodorsen functions. The two cross sections show streamlined-

body aerodynamic characteristics. A_2^* is always negative and decreases with the increasing $U/(f \cdot B)$, so the uncoupled self-excited pitching moment generates positive damping. The negative damping is provided by the coupled term $H_3^* A_1^*$, which is the main contributing source driving the bridge to the coupled flutter instability. For the two cases, the flutter frequencies are between the vertical and torsional natural frequencies, and the critical flutter wind speeds are relatively high. The rectangle with $B/H=10$ shows bluff-body aerodynamic characteristics. A_2^* first decreases, but then changes its sign from negative to positive at higher wind speeds. In this situation, the uncoupled self-excited pitching moment would generate negative damping, driving the bridge to the torsional flutter instability. The critical flutter wind speed decreases seriously.



(a) 0° angle of attack

(b) 4° angle of attack

(c) 8° angle of attack

Fig. 2 Flutter derivatives of different cross sections at different angles of attack

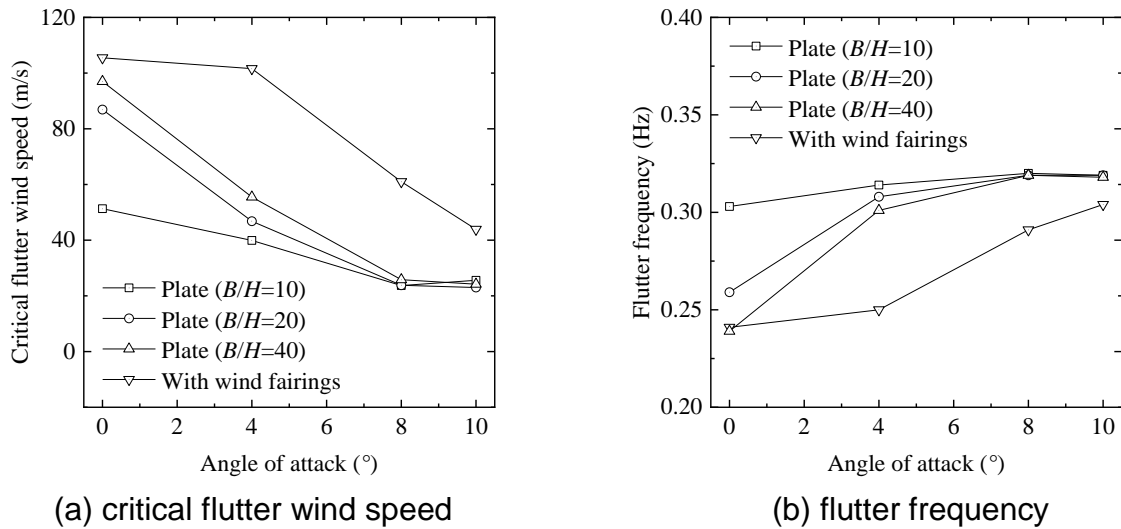


Fig. 3 Critical flutter state of the long-span suspension bridge

With the increasing angle of attack, A_2^* of the rectangles with $B/H=40$ and 20 also becomes positive. In other words, the rectangle with a larger B/H could also show bluff-body aerodynamic characteristics at large angles of attack, leading to reduction of the flutter performance.

After adding the wind fairings on the two side of the rectangle ($B/H=10$), the variations of the flutter derivatives trend to the Theodorsen functions, especially at 0° and 4° angles of attack. The critical flutter wind speed of the bridge is largely improved. It can be seen that the wind fairing is very favorable to the flutter performance of the bridge at both small and large angles of attack. The average percentage change in the critical flutter wind speed is 122.3%.

2.3 Effects of wind fairings

Although the wind fairing could improve the flutter performance of the bridge, an optimal shape is necessary to further improve the flutter performance at large angles of attack. In the previous study, the angle of the wind fairing φ was set to 60° . Here, the angle was decreased to 40° , 50° , and increased to 70° , 80° , respectively. Two angles of attack of incoming flow, i.e., 8° and 10° , were selected. Fig. 4 shows the cross sections of the box girders with different wind fairings. For $\varphi = 180^\circ$, the wind fairing is not included, i.e., the rectangle with $B/H=10$.

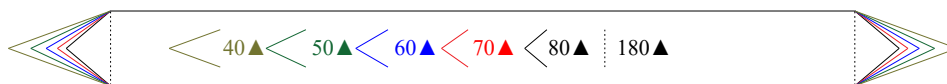


Fig. 4 Box girders with different wind fairings

Similarly, SDOF heaving and torsional harmonic vibrations were imposed to extract the flutter derivatives, and the results are shown in Fig. 5. The critical flutter

state of the suspension bridge in different cases was also calculated via the two degree-of-freedom flutter analysis method. The critical flutter wind speed and the flutter frequency of the bridge are shown in Fig. 5. For the flutter derivatives H_3^* and A_1^* , the variations approach to the Theodorsen functions when the box girder is equipped with a blunt wind fairing (i.e., $\varphi=80^\circ$). For the flutter derivative A_2^* , the variation approaches to the Theodorsen function when the box girder is equipped with a sharp wind fairing (i.e., $\varphi=40^\circ$). As the torsional flutter instability occurs at large angles of attack, A_2^* is closely related to the flutter performance. With the decreasing angle of the wind fairing from 80° to 40° , the flutter frequency decreases from 0.32 to 0.275 Hz. Comparing with the symmetrical vertical and torsional modal frequencies of the bridge, i.e., 0.153 Hz and 0.325 Hz, the torsional flutter of the bridge has converted to the coupled bending-torsional flutter, and the critical flutter wind speed increases.

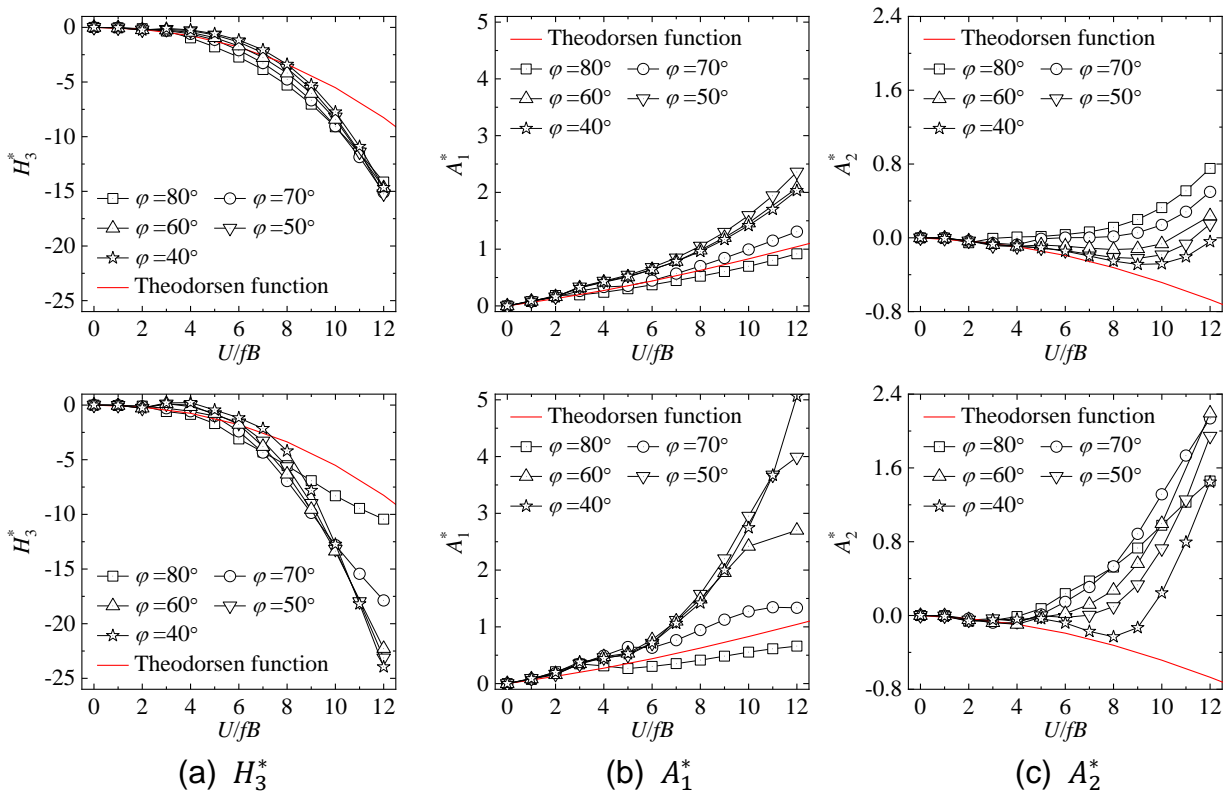


Fig. 5 Flutter derivatives of box girders with different wind fairings

Table 2 Critical flutter state of a long-span suspension bridge

Angle of the wind fairing ($^\circ$)		40	50	60	70	80	180
Critical flutter wind speed (m/s)	$\alpha=8^\circ$	67.0	63.7	61.0	46.0	32.0	23.7
	$\alpha=10^\circ$	56.3	47.8	43.9	37.2	32.0	25.6
Flutter frequency (Hz)	$\alpha=8^\circ$	0.275	0.282	0.291	0.312	0.320	0.320
	$\alpha=10^\circ$	0.285	0.298	0.304	0.312	0.317	0.319

2.4 Flow field characteristics

In this section, dynamic flow field characteristics around the girder are studied to understand how the wind fairing improves the flutter performance of the bridge. Fig. 6 shows the static pressure contours around the rectangle girder in one torsional cycle with $U/fB=6$ and 8° angle of attack. Four cycle instants are selected to draw the pictures. Between two adjacent instants, the input energy by the pitching moment acting on the girder is computed and marked in Fig. 14. When the girder rotates clockwise from the equilibrium position to the maximum amplitude, the vortex formed above the girder quickly becomes bigger and stronger. The pitching moment has the clockwise direction and produces positive energy (5.04×10^{-4} J) which promotes the torsional vibration of the girder. When the girder rotates counter-clockwise from the maximum amplitude to the minimum amplitude, the vortex above the girder is supposed to inhibit the torsional vibration of the girder. In fact, the vortex soon flows downstream and separates from the girder. The direction of the pitching moment becomes counter-clockwise, so the input energy during this process is still positive ($-2.78 \times 10^{-5} + 2.19 \times 10^{-4}$ J). Finally, the girder rotates clockwise from the minimum amplitude to the next equilibrium position. The vortex above the girder is formed again gradually. As the computed wind speed ($U/fB=6$) exceeds the critical flutter wind speed ($U/fB=2.74$), the total input energy by the pitching moment during one torsional cycle is positive, i.e., 7.96×10^{-4} J, and the torsional amplitude of the girder will increase.

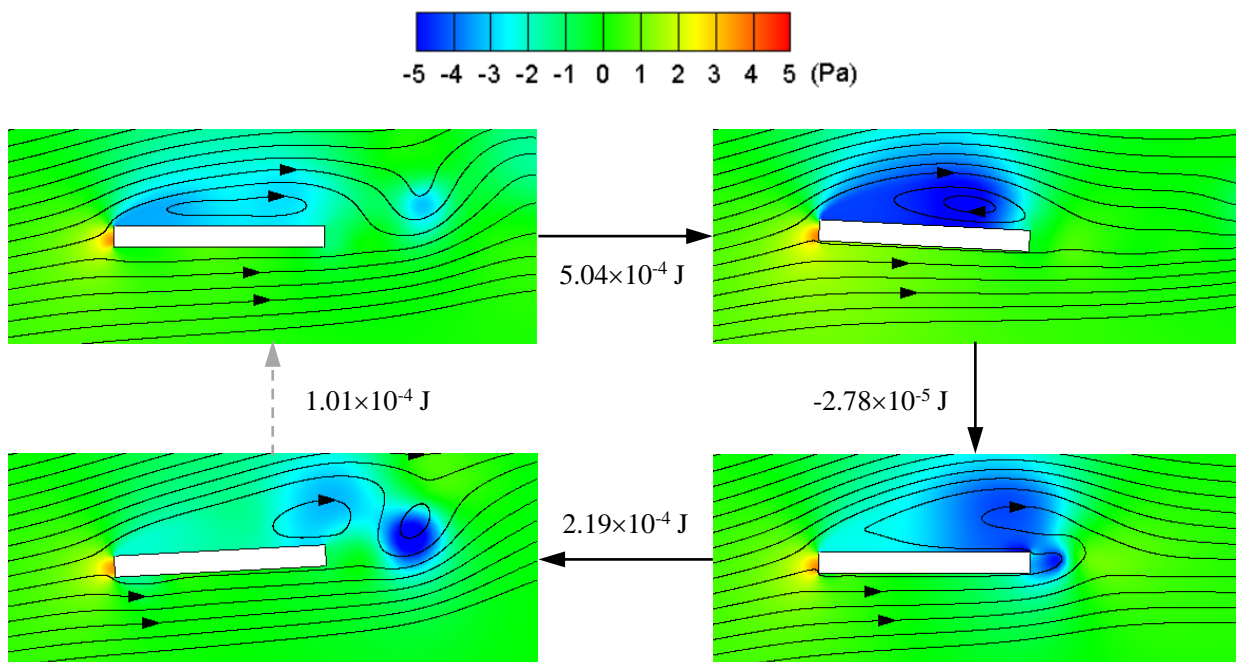


Fig. 6 Contours of the static pressure around the rectangle girder

After installing wind fairings on the rectangle girder, the flow field characteristics change significantly, as shown in Fig. 7. When the girder rotates clockwise, the size of the vortex above the girder becomes small. When the girder rotates counterclockwise,

the movement of the vortex towards downstream side is restricted by the windward wind fairing. During the counterclockwise vibration of the girder, the pitching moment keeps the opposite direction, so it produces negative energy on the girder. With the decreasing angle of the wind fairing from 80° to 40° , the restriction on the vortex is enhanced. The total input energy during one torsional cycle decreases, and the sign changes from positive to negative, i.e., 1.45×10^{-4} J, -4.70×10^{-4} J, and -1.01×10^{-3} J for the three cases, respectively. With a negative energy, the current vibration cannot be maintained, so the flutter instability may occur at a higher wind speed.

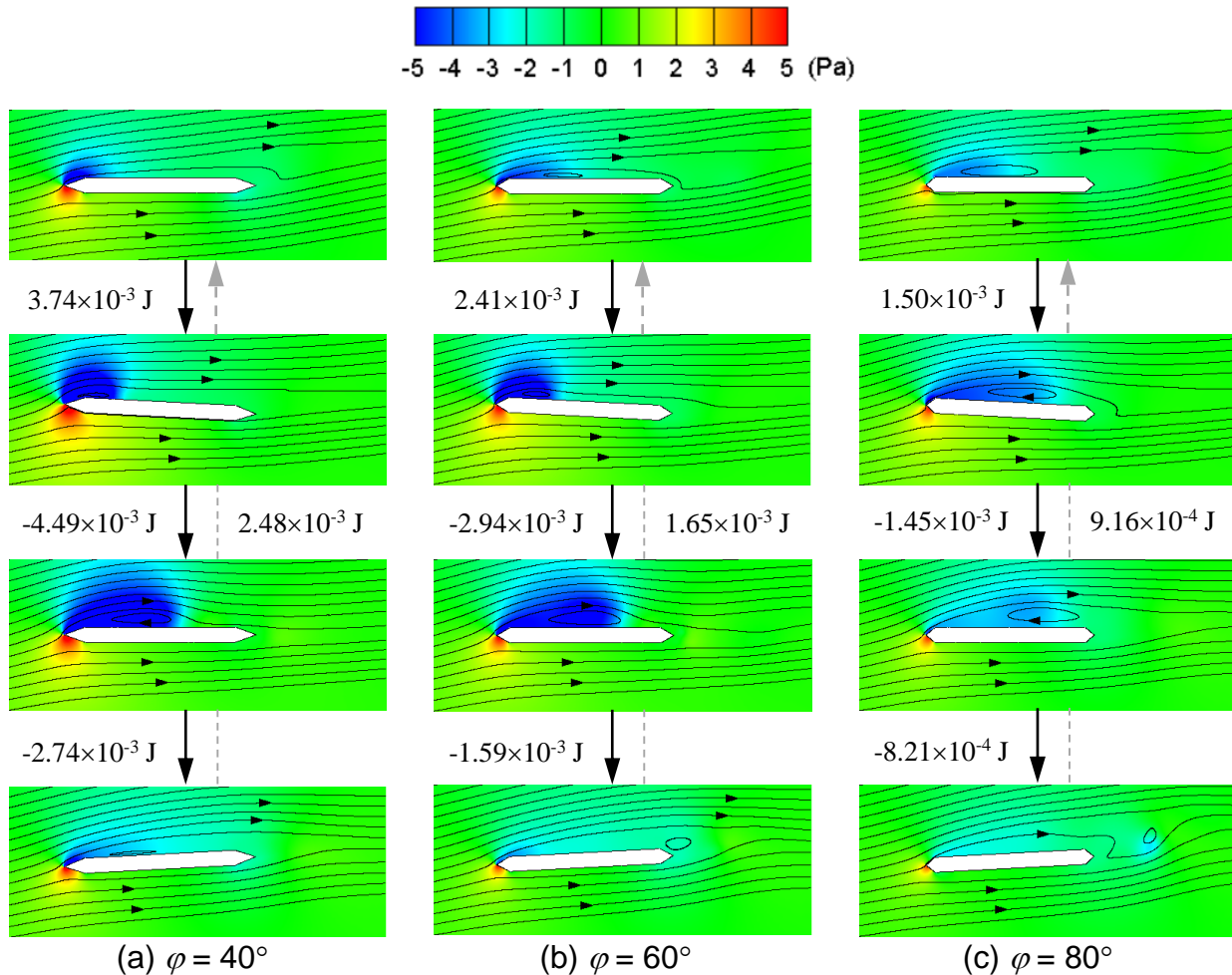


Fig. 7 Contours of the static pressure around different box girders

3. CONCLUSIONS

The flutter performance of box girders with different wind fairings at large angles of attack is investigated. The dynamic flow field characteristics around the girder are studied to discuss how the wind fairing improves the flutter performance of the bridge at large angles of attack. The following main conclusions are made, which provides reference for the improvement of the flutter performance of box girders.

A girder is easier to show bluff-body aerodynamic characteristics at a larger angle of attack, leading to reduction of the flutter performance. Installing the wind fairing is favorable to the flutter performance of the bridge at both small and large angles of attack. At large angles of attack, the sharper wind fairing could further improve the flutter performance of bridge, as the variation of the flutter derivative A_2^* is closer to the Theodorsen function and the critical flutter wind speed increases. The probable reason is that the adverse effects of the vortex, which may drive the bridge to torsional flutter instability at large angles of attack, are weakened by the wind fairing.

REFERENCES

- Bilal, M., Birkelund, Y., Homola, M., and Virk, M. S., (2016), "Wind over complex terrain – Microscale modelling with two types of mesoscale winds at Nygårdstjøll", *Renewable Energy*, 99, 647–653.
- Blocken, B., van der Hout, A., Dekker, J., and Weiler, O., (2015), "CFD simulation of wind flow over natural complex terrain: Case study with validation by field measurements for Ria de Ferrol, Galicia, Spain", *Journal of Wind Engineering and Industrial Aerodynamics*, 147, 43–57.
- Chen, X., Guo, J., Tang, H., Li, Y. and Wang, L. (2020), "Non-uniform wind environment in mountainous terrain and aerostatic stability of a bridge", *Wind Struct.*, **30**(6), 649-662.
- Fenerci, A., Øiseth, O., Rønquist, A., 2017. Long-term monitoring of wind field characteristics and dynamic response of a long-span suspension bridge in complex terrain. *Engineering Structures*. 147, 269-284.
- Hui, M. C. H., Larsen, A., and Xiang, H. F., (2009), "Wind turbulence characteristics study at the Stonecutters Bridge site: Part I—Mean wind and turbulence intensities", *Journal of Wind Engineering and Industrial Aerodynamics*, 97(1), 22–36.
- Larsen A. (1993) Aerodynamic aspects of the final design of the 1624 m suspension bridge across the Great Belt. *Journal of Wind Engineering and Industrial Aerodynamics* 48(2–3): 261–285.
- Lee, S., Kwon, S.D., Yoon, J., 2014. Reynolds number sensitivity to aerodynamic forces of twin box bridge girder. *Journal of Wind Engineering and Industrial Aerodynamics*. 127, 59-68.
- Li, Y.L., Xu, X.Y., Zhang, M.J., Xu, Y.L., 2017a. Wind tunnel test and numerical simulation of wind characteristics at a bridge site in mountainous terrain. *Advances in Structural Engineering*. 20(8), 1223-1231.
- Li, Y.L., Hu, P., Xu, X.Y., Qiu, J.J., 2017b. Wind characteristics at bridge site in a deep-cutting gorge by wind tunnel test. *Journal of Wind Engineering and Industrial Aerodynamics*. 160, 30-46.
- Ma C, Duan Q, and Liao H. (2018) Experimental Investigation on Aerodynamic Behavior of a Long Span Cable-stayed Bridge Under Construction. *KSCE Journal of Civil Engineering* 22(7): 2492–2501.
- Syrkov AV, and Krutikov OV. (2014) Lifecycle optimization for Vladivostok-Russky isle bridge by means of risk analysis and monitoring. *Automation and Remote Control* 75(12): 2217–2224.

*The 2020 World Congress on
Advances in Civil, Environmental, & Materials Research (ACEM20)
25-28, August, 2020, GECE, Seoul, Korea*

- Tang, H., Li, Y., Shum, K.M., Xu, X. and Tao, Q. (2020), "Non-uniform wind characteristics in mountainous areas and effects on flutter performance of a long-span suspension bridge", *J. Wind Eng. Ind. Aerod.*, **201**, 104177.
- Tao T, Wang H, Yao C, et al. (2017) Parametric Sensitivity Analysis on the Buffeting Control of a Long-Span Triple-Tower Suspension Bridge with MTMD. *Applied Sciences* 7(4): 395.
- Zhang, Z.T., Ge, Y.J., Yang, Y.X., 2013. Torsional stiffness degradation and aerostatic divergence of suspension bridge decks. *Journal of Fluids and Structures*. 40, 269-283.
- Zhu, Q., Xu, Y.L., 2014. Characteristics of distributed aerodynamic forces on a twin-box bridge deck. *Journal of Wind Engineering and Industrial Aerodynamics*. 131, 31-45.